Equivalent Circuit Analysis of a Nonlinear Vortex-Induced Vibration Piezoelectric Energy Harvester Using Synchronized Switch Technique

Junlei Wang, Liangjun Luo, Daniil Yurchenko, and Guobiao Hu

***Abstract*—Introducing nonlinearity into vortex-induced vibration (VIV) piezoelectric energy harvesters (PEHs) can enlarge bandwidths and improve energy harvesting efficiency. Through the analogy between mechanical and electrical domains, the mechanical model of the PEH can be equivalently represented by a circuit model, and the influences of the interface circuits on the energy harvester effect can be studied more conveniently. In this article, a magnetically coupled nonlinear VIVPEH prototype is first developed and tested in the wind tunnel. Second, the equivalent circuit model is established to study the performance of nonlinear VIVPEH. The simulation results are compared with the experimental ones for verification. Finally, the nonlinear VIVPEH is shunted to a simple ac circuit, a standard dc circuit, and SSHI interface circuits to investigate the effects of different interface circuits. The results show that the bistable nonlinear structure can increase the working bandwidth of the VIVPEH, indicating at least an 114.3% improvement over the monostable one. The P-SSHI circuit interface can effectively increase the average power output of the VIVPEH by 65.04% and 174.32% compared to the ac and dc circuits. The work in this article provides valuable insights and guidelines for designing efficient nonlinear VIVPEHs using magnetic coupling and advanced interface circuits.**

***Index Terms*—Equivalent circuit model (ECM), interface circuits, magnetic coupling, piezoelectric energy harvesting, vortex-induced vibration (VIV).**

Received 9 September 2024; revised 24 September 2024; accepted 28 September 2024. Date of publication 29 October 2024; date of current version 3 April 2025. This work was supported by the National Natural Science Foundation of China under Grant 52277227 and Grant 52305135, in part by the Guangzhou Municipal Science and Technology Project under Grant 2023A03J0011, in part by the Guangdong Provincial Key Lab of Integrated Communication, Sensing and Computation for Ubiquitous Internet of Things under Grant 2023B1212010007, and in part by the Guangzhou Municipal Key Laboratory on Future Networked Systems under Grant 024A03J0623. *(Corresponding author: Guobiao Hu.)*

Junlei Wang and Liangjun Luo are with the School of Mechanical and Power Engineering, Zhengzhou University, Zhengzhou 450000, China (e-mail: jlwang@zzu.edu.cn; luolj@gs.zzu.edu.cn).

Daniil Yurchenko is with the School of Institute of Sound and Vibration Research, University of Southampton, SO17 1BJ Southampton, U.K. (e-mail: d.yurchenko@soton.ac.uk).

Guobiao Hu is with the Internet of Things Thrust, The Hong Kong University of Science and Technology (Guangzhou), Nansha, Guangzhou, Guangdong 511400, China (e-mail: guobiaohu@hkust-gz.edu.cn).

Digital Object Identifier 10.1109/TIE.2024.3476923

I. Introduction

THE aerodynamic instability phenomena known as flow-induced vibration (FIV) are caused by fluid-structure interactions (FSIs) as the flow passes through structures. Over the past decade, there has been a surge in research efforts to explore FIV energy harvesting [1], [2]. Various mechanisms lead to the categorization of FIV into different types, such as vortex-induced vibration (VIV) [3], [4], galloping [5], [6], flutter [7], [8], and buffeting [9], [10]. Bluff bodies play a crucial role in the onset of FIV, and different types of bluff bodies can induce distinct aeroinstabilities. Wang et al. [11] designed a VIV piezoelectric energy harvester (PEH) with a Y-shaped attachment and compared it with the one having a smooth cylindrical surface. It was found that by introducing the Y-shaped attachment, VIV could be transformed into galloping, leading to an enhancement in energy harvesting performance. Barrero-Gil et al. [12] tested 17 bluff bodies with different cross-section shapes while ensuring the same mechanical properties and aspect ratio. Their conclusion suggested cross-section shapes with high-energy transfer efficiency could be predesigned using two related dimensionless geometric parameters. Xing et al. [13] proposed 3-D printed 16 square-sectioned bluff bodies with different aspect ratios and leeward protrusion lengths and investigated their coupling effects on the performance of VIV-galloping energy harvesters.

In addition to optimizing the aerodynamics of bluff bodies, efforts have also been devoted to developing mechanical structures to alter the dynamic behavior. For example, introducing nonlinearities into PEH systems can overcome the shortcomings of the narrow bandwidths of linear energy harvesters and provoke larger amplitude responses. Nonlinear stiffness can be achieved through two typical means: geometric nonlinearity and magnetic coupling [14], [15], [16]. Geometric nonlinearities can be realized by implementing the connections with linear springs [17] and beams [18]. Magnetic coupling can be realized by introducing magnets to linear energy harvesting systems. The attraction or repulsion between the magnets can generate nonlinear forces, transforming linear systems into nonlinear ones. Researchers have studied nonlinear FIV piezoelectric energy harvesting systems under magnetic coupling [19], [20]. He et al. [21] proposed a novel low frequency, noncontact magnetically coupled PEH that can effectively harvest energy from ocean

wave energy. Experiments show that the device can light up 16 light-emitting diodes under the excitation of a water flow rate of 1.6×10^4 L/h. Han et al. [22] developed a novel composite piezoelectromagnetic synchronous energy supply and sensing device (P-ESSD) for vehicle monitoring. The device can convert the wasted energy in urban traffic congestion into electricity and realize self-energy supply and self-sensing function.

Previous investigations into piezoelectric energy harvesting typically focused on either the mechanical or electrical perspective. Yang and Tang [23] established an equivalent circuit model (ECM) to bridge the structural modeling and electrical circuit simulation. Tao et al. [24] designed a novel MEMS energy harvester based on electrostatic film by combining a multimodal structure and shock-induced nonlinearity. Experiments and circuit simulations confirm that it has superior energy harvesting efficiency and bandwidth expansion ability at low to medium excitation levels. Tang et al. [25] developed an ECM representation method to predict the performance of GPEH and evaluated the performance of a GPEH shunted to ac and dc interface circuits. Some researchers attempted to improve the performance of vibration energy harvesters by optimizing the interface circuit. Zhao et al. [26] revealed three advantages of the SCE circuit for GPEH. In 2005, Guyomar et al. [27] first proposed a synchronous switch harvesting interface (SSHI) circuit for energy harvesting systems. Zhao et al. [28] conducted wind tunnel experiments for a GPEH and compared the performance of a series SSHI circuit (S-SSHI) and a parallel SSHI circuit (P-SSHI), as well as a standard interface circuit. The results indicated that the advantages of the SSHI circuit become more noticeable at high-wind speeds, and the output power of P-SSHI increased from 1.6 to 2.3 mW compared with the standard circuit, representing a 43.75% increase. Lien et al. [29] uncovered the influence of frequency deviation resonance on the electrical behavior of the SSHI system. All the above studies are limited to the consideration of advanced interface circuits for GPEHs. One major reason is the lack of a general equivalent circuit modeling method for VIVPEHs. In 2019, Wang et al. [30] developed an ECM for a typical VIVPEH for the first time. They evaluated the VIVPEH when being shunted to different ac and dc circuits. The results showed that the efficiency of the ac interface was greater than that of the dc interface under a specific optimal load. Jia et al. [31] also developed an ECM for a VIVPEH and considered a dc interface circuit. They validated the ECM using experimental test results. Using different types of switching interface circuits can enhance the energy harvesting capability, but it has little effect on the bandwidth. The introduction of nonlinear magnetic force can obviously broaden the working bandwidth, but it is difficult to increase the amplitude stably. However, if the two advantages can be combined, it will significantly improve the efficiency of capturing energy.

In general, researchers have introduced nonlinear magnetic force into FIVEHs and applied equivalent circuit modeling methods to study their behaviors. However, the influences of those interface circuits on the performance of nonlinear VIVPEHs have not been fully understood. Therefore, to fill this gap, this article first proposed a more general ECM for VIVPEHs and validated its correctness through experiments. Subsequently, an SSHI interface circuit is considered based on the developed ECM. The influences of different interface circuits on the output responses of the nonlinear VIVPEH are studied. The performance of a simple ac circuit, a standard dc circuit, and SP-SSHI circuits are evaluated and compared.

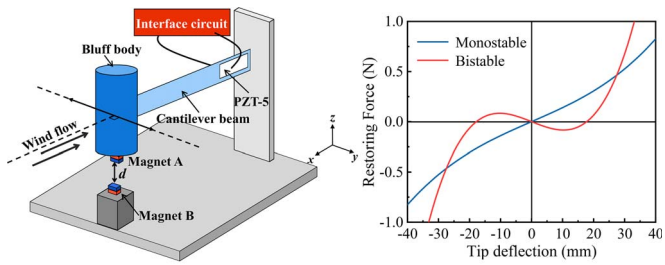

Fig. 1. (a) Configuration of the nonlinear VIVPEH and (b) nonlinear restoring force.

II. System Outline

A. Mechanical Structure

Fig. 1(a) shows the structure of the proposed nonlinear VIVPEH. One end of the cantilever beam is fixed on the rigid support, and the other is attached with a cylinder bluff body. A piezoelectric patch (PZT-5) is bonded on the cantilever beam near the clamped end. The mechanism of VIV involves the generation of vortices in the wake of the bluff body. These vortices can interact with the structure, causing it to vibrate. When the vortex shedding frequency is close to the natural frequency of the VIVPEH, known as the frequency "lock-in" phenomenon, the VIVPEH will carry out a large amplitude vibration and generate substantial power output. The vortex-shedding frequency $\omega_{VIV} = 2\pi S_t U/D$, where D is the diameter of the bluff body, U is the incoming wind speed, and S_t is the Strouhal number, which depends on the surface roughness of the bluff body and the Reynolds number that signifies the viscosity of the fluid.

The nonlinear force is incorporated by attaching a magnet to the bottom of the bluff body and fixing another vertically to the rigid base. The two magnets are configured to exert a repulsive force. By varying the distance between the two magnets, the harvester may exhibit monostable or bistable behavior. Typical nonlinear restoring forces of monostable and bistable harvesters are shown in Fig. 1(b). The nonlinear restoring force can be described by a cubic polynomial $F_k = k_1 y + k_3 y^3$, where y is the displacement of the bluff body along the y-direction.

B. Interface Circuits

To facilitate the study of such electromechanically coupled systems, researchers established analogies between mechanical and circuit elements based on comparing their governing differential equations. By utilizing this method, a general PEH can be represented by an equivalent circuit. Thus, the entire system, including the PEH and the shunted interface circuit, can be built and simulated using circuit simulation software. For simplicity, researchers in the mechanical background often shunt the PEH to a pure resistor (simple ac circuit, deemed as the load), as

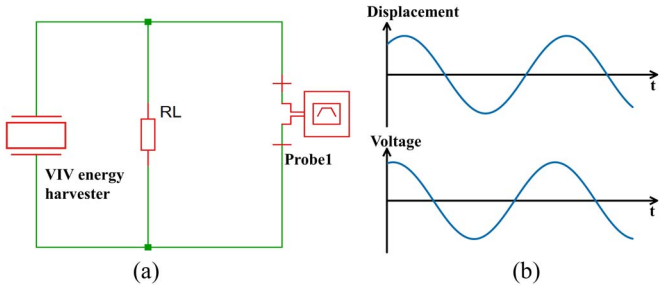

Fig. 2. (a) Schematic of the simple ac interface circuit and (b) corresponding waveforms of the tip displacement and the output voltage.

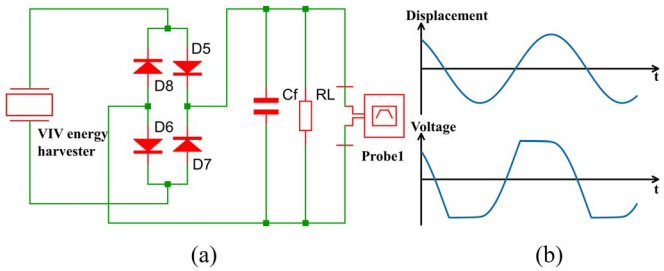

Fig. 3. (a) Schematic of the standard dc interface circuit and (b) corresponding waveforms of the tip displacement and the output voltage.

shown in Fig. 2(a). Fig. 2(b) shows the time-history waveforms of the displacement of the bluff body and the voltage across the piezoelectric transducer V_p when the PEH is shunted to an ac interface circuit. V_p is obtained by placing a differential voltage probe on the two ends of the piezoelectric capacitor C_p; and the displacement measurement method will be described in detail later. As can be seen, both curves are sinusoidal, but their phases are not synchronized, and this phase difference is influenced by the load resistance, piezoelectric capacitance, and excitation frequency. For the case using an ac interface circuit, the voltage output generated by the PEH is an electrical signal that varies in magnitude and direction over time. However, most electronic devices we use daily require dc power supplies. Therefore, using a rectifier bridge to realize ac–dc conversion is very essential. In addition, a filter capacitor is required to stabilize the pulsating dc voltage that directly flows out of the rectifier. Finally, one can connect an electronic device (typically denoted by a load resistor for simplicity) in parallel with the filter capacitor for practical utilization. Such a circuit, as shown in Fig. 3(a), is referred to as the standard dc interface circuit. The waveform of V_p in Fig. 3(b) is different from the sine curve of the displacement. In the beginning, before the steady state, the PEH as a power source transfers energy to C_f and R_L, and during this period $V_p = V_{RL}$. After a while, when the energy stored on C_f is saturated, the voltage will fluctuate around V_f. During each cycle, the energy input into C_f balances with the energy consumed by the load resistance. In short, the filter capacitor C_f absorbs and releases energy to maintain a relatively stable output voltage.

As an electromechanical system, interface circuits greatly influence the energy harvesting efficiency of a PEH [32], [33]. The self-powered S-SSHI circuit shown in Fig. 4(a) consists of discrete electronic components, with R_1, D_1, and C_1 constituting the envelope detector and T_1 and T_3 acting as a comparator and an electronic switch, respectively. The piezoelectric voltage waveform is shown in Fig. 4(b). The piezoelectric device can be modeled as a structure with an equivalent current source and a piezoelectric capacitor C_p in parallel. A cycle is roughly divided into four stages: at the beginning, the current flows to the piezoelectric capacitor, and then C_p, C_1, and C_2 are charged naturally, V_p reaches its maximum voltage $V_{\max}$; when $V_p = V_1$, the transistor T_1 is switched on, C_1 starts discharging, T_3 is switched on, and L starts charging; Then the current through L tends to reverse its flow direction, and the emitter-collector capacitor

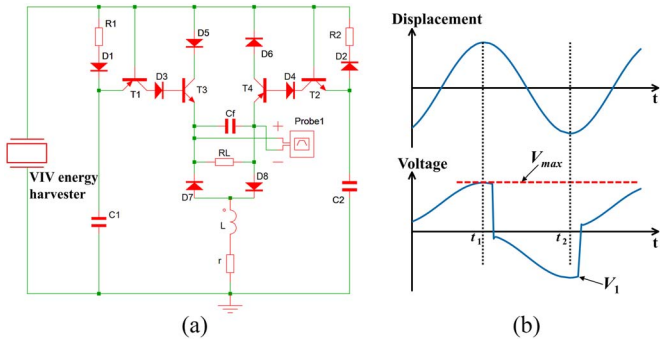

Fig. 4. (a) Schematic of the S-SSHI interface circuit and (b) corresponding waveforms of the tip displacement and the output voltage.

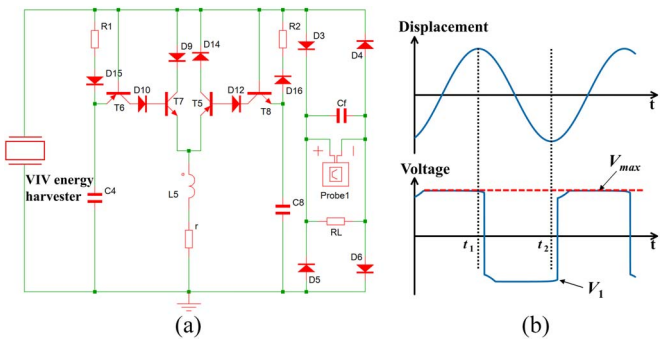

Fig. 5. (a) Schematic of the P-SSHI interface circuit and (b) corresponding waveforms of the tip displacement and the output voltage.

C_{CE} of T_4 is charged; Finally, the remaining charge in C_2 flows into C_p and C_1 until their voltages are equal. Fig. 5 presents the P-SSHI interface circuit and its corresponding waveforms. Compared with the S-SSHI circuit, the layout of the P-SSHI circuit is changed. The load resistance, filter capacitor, and rectifier bridge are connected in parallel, unlike the S-SSHI circuit. Nevertheless, the working principle of the P-SSHI is similar. Thus, there is no need for further elaboration. The two circuits are self-powered and do not require external power supplies to control the switches. In this article, the energy harvesting characteristics of different interface circuits are analyzed efficiently through circuit simulation. At the same time, it is worth noting that some electronic elements used in circuit simulation are ideal. However, the energy loss incurred by the passive electronic elements in practical applications cannot be ignored.

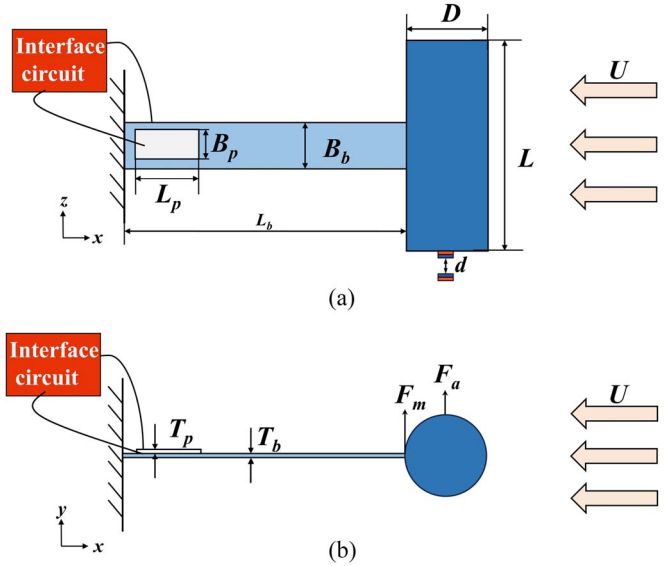

Fig. 6. Geometric schematic of the nonlinear VIVPEH: (a) top view; and (b) front view.

III. Theoretical Modeling

A. Aeroelectromechanical Model

Fig. 6 shows the top and front views of the VIVPEH with nonlinear force introduced. It is composed of a cylindrical bluff body, a cantilever beam, a piezoelectric sheet, and two small magnets. The diameter and the height of the bluff body are, respectively, D and L. The cantilever beam has a length of L_b, a width of B_b, and a thickness of T_b. The length, width, and thickness of the piezoelectric sheet are L_p, B_p, and T_p, respectively. The nonlinearity is achieved by attaching one magnet at the bottom of the bluff body and fixing the other to a rigid bracket placed in parallel. The two magnets are identical in shape and size, but their poles are arranged opposite to produce a repelling force. The distance between the two magnets is d. Under a uniform airflow with a constant velocity of U that falls into a specific range, the aerodynamic force produced on the bluff body will drive the beam to vibrate periodically in the y-direction.

The slender beam theory, i.e., the Euler Beam theory, is utilized to derive the governing equation of the beam with a piezoelectric layer, as the length of the beam in this study far exceeds its thickness. By following the standard procedures [34], [35], i.e., using modal superposition and modal orthogonality, we can finally obtain the governing equation in the modal coordinate form

$$\ddot{\eta}(t) + 2\xi\omega_n\dot{\eta}(t) + \omega_n^2\eta(t) + \chi V(t) = F_{\mathrm{VIV}}(t) \tag{1}$$

where $\eta(t)$ represents the modal coordinate; ξ denotes the damping ratio, which can be generally measured by a free decay test; ω_n denotes the natural frequency; χ is the modal electromechanical coupling coefficient; $V(t)$ denotes the voltage across the load resistance; and $F_{\mathrm{VIV}}(t)$ represents the VIV aerodynamic force that can be further expressed using the below empirical formula

$$f_{\mathrm{VIV}}(t) = \frac{1}{2}\rho C_L DLU^2\varphi(L_b) - \frac{1}{2}\rho C_D DLU\varphi^2(L_b)\dot{\eta}(t) \tag{2}$$

where ρ is the fluid density, $C_L = C_{L0}q(t)/2$ is the fluctuating lift coefficient, and C_{L0} is the amplitude; U is the flow velocity, $\varphi(x)$ is the first-order modal shape of the piezoelectric beam; and C_D is the average drag coefficient, which can be obtained in the CFD simulation. $q(t)$ is a variable to describe the motion of the near wake whose dynamic behavior is assumed to follow the van der Pol wake oscillator model. Thus, the governing equation can be written as

$$\ddot{q}(t) + \lambda\omega_{\mathrm{VIV}}[q^2(t) - 1]\dot{q}(t) + \omega_{\mathrm{VIV}}^2 q(t) = \frac{A}{D}\varphi(L_b)\ddot{\eta}(t) \tag{3}$$

where $\lambda = 0.3$ and $A = 1.2$, which are experimentally determined parameters [36], and ω_{VIV} is calculated according to the vortex shedding frequency f_{VIV}, $\omega_{\mathrm{VIV}} = 2 \times \pi \times f_{\mathrm{VIV}}$, where $f_{\mathrm{VIV}} = \mathrm{St} \times U/D$. St is the Strouhal number.

By shunting the piezoelectric transducer to a resistive load R_L, the circuit governing equation can be established as

$$\frac{V(t)}{R_L} + C_p\dot{V}(t) - \chi\dot{\eta}(t) = 0 \tag{4}$$

where C_p is the internal capacitance of the piezoelectric transducer.

Combining (1)–(4) and using the equivalent lumped parameter representation $M_{\mathrm{eff}} = 1/\varphi^2(L_b)$, $C_{\mathrm{eff}} = 2\xi\omega_n/\varphi^2(L_b)$, $K_{\mathrm{eff}} = \omega_n^2/\varphi^2(L_b)$, $\theta = \chi/\varphi(L_b)$, $y(t) = \varphi(t)/\eta(t)$, one can eliminate the modal terms. The governing equations of the VIVPEH represented in the SDOF form are then obtained as follows:

$$M_{\mathrm{eff}}\ddot{y}(t) + \left[\frac{1}{2}\rho DLUC_D + C_{\mathrm{eff}}\right]\dot{y}(t) + K_{\mathrm{eff}}y(t) + \theta V(t) = \frac{1}{4}\rho C_{L0}DLU^2 q(t) \tag{5}$$

$$\ddot{q}(t) + \lambda\omega_{\mathrm{VIV}}[q^2(t) - 1]\dot{q}(t) + \omega_{\mathrm{VIV}}^2 q(t) = \frac{A}{D}\ddot{y}(t) \tag{6}$$

$$\frac{V(t)}{R_L} + C_p\dot{V}(t) - \theta\dot{y}(t) = 0 \tag{7}$$

where M_{eff} is the equivalent mass, $M_{\mathrm{eff}} = 33/140m_1 + m_2$ [37], [38], where m_1 is the mass of the beam, and m_2 represents the combined mass of the tip attachment, encompassing the bluff body and the attached magnet. K_{eff} is the equivalent stiffness, $C_{\mathrm{eff}} = 2\xi\omega_n M_{\mathrm{eff}}$ is the equivalent damping coefficient, and θ is the electromechanical coupling coefficient. $y(t)$ is the displacement of the bluff body.

Compared with traditional VIVPEHs, the one proposed in this article incorporates a nonlinear magnetic force $F_r(y)$. Therefore, the governing equation of the proposed nonlinear VIVPEH can be obtained by replacing the linear restoring force in (5) with a nonlinear one

$$M_{\mathrm{eff}}\ddot{y}(t) + \left[\frac{1}{2}\rho DLUC_D + C_{\mathrm{eff}}\right]\dot{y}(t) + F_r(y) + \theta V(t) = \frac{1}{4}\rho C_{L0}DLU^2 q(t) \tag{8}$$

where $F_r(y) = k_1 y(t) + k_3 y^3(t)$, k_1 and k_3 are the coefficients of the linear and cubic terms. The nonlinear force applied on the bluff body by the stationary magnet can be measured in the experiment using a dynamometer. Then, a fitting curve can be found to explicitly express $F_r(y)$.

TABLE I
ANALOGIES BETWEEN MECHANICAL AND ELECTRICAL COMPONENTS

Mechanical Variables/Components	Electrical Variables/Components
Force: F	Voltage: V
Displacement: $y(t)$	Charge: $q(t)$
Velocity: $\dot{y}(t)$	Current: $\dot{q}(t)$
Acceleration: $\ddot{y}(t)$	Rate of current change: $\ddot{q}(t)$
Effective damping: C_{eff}	Resistance: R
Effective mass: M_{eff}	Inductance: L
Reciprocal of effective stiffness: $1/K_{\text{eff}}$	Capacitance: C
Electromechanical coupling: Θ	Ideal transformer turn ratio: N

B. Equivalent Circuit Model

Though many different ECMs have been established for harvesters with different features, there still is a lack of an ECM tailored specifically for VIVPEHs due to complex dynamics. The VIVPEH proposed in this article consists of multiple components, including a beam structure, a piezoelectric transducer, two magnets, a bluff body, and an interface circuit. This section presents the development of the ECM of the VIVPEH using the analogies between mechanics and electricity.

Using the analogies between the electrical and mechanical elements as summarized in Table I, (6)–(8) can be rewritten as

$$\begin{cases} L\ddot{q}_1(t) + R\dot{q}_1(t) + k_1 q_1(t) + k_3 q_1^3(t) + NV(t) \\ \qquad = \dfrac{1}{4}\rho C_{L0} DLU^2 q_2(t) - \dfrac{1}{2}\rho DLUC_D \dot{q}_1(t) \\ \ddot{q}_2(t) + \lambda\omega_{\text{VIV}}[q_2{}^2(t) - 1]\dot{q}_2(t) + \omega_{\text{VIV}}^2 q_2(t) = \dfrac{A}{D}\ddot{q}_1(t) \\ \dfrac{V(t)}{R_L} + C_p\dot{V}(t) - N\dot{q}_1(t) = 0 \end{cases} \tag{9}$$

where $q_1(t) = y(t) = C_1 \times V_{C1}$ is the displacement of the bluff body, and its electrical analogy is the charge flowing in one loop of the circuit model, $q_2(t) = q(t) = C_2 \times V_{C2}$ as defined in (3). We can then establish a circuit model, as shown in Fig. 7, that follows the governing equations in (9).

The four blocks, i.e., ARB1, ARB2, ARB3, and ARB4 in Fig. 7, are user-defined arbitrary sources, respectively, represent the aerodynamic force, the inertial force applied on the wake oscillator, the nonlinear damping term in the wake oscillator's governing equation, and the magnetic force. Specifically, the four arbitrary sources are defined as

$$\begin{cases} \text{ARB1} = \dfrac{1}{4}\rho C_{L0} DLU^2 C_1 V_{C1} - \dfrac{1}{2}\rho DLUC_D I(\text{iin}) \\ \text{ARB2} = \dfrac{A}{D}\dfrac{V_L}{L} \\ \text{ARB3} = \lambda\omega_{\text{VIV}}[(C_2 V_{C2})^2 - 1]I(\text{iin}) \\ \text{ARB4} = -\{(k_1 - K_{\text{eff}})C_1 V_{C1} + k_3(C_1 V_{C1})^3\}. \end{cases} \tag{10}$$

In ARB1 and ARB3 modules, although both use I(iin), the currents they represent are different. In ARB1, I(iin) $= \dot{q}_1(t)$, in ARB3, I(iin) $= \dot{q}_2(t)$. In general, I(iin) universally represents the current in a circuit loop. Then, the "current differentiator" module in the figure is used to generate an output voltage proportional to the rate of the input current change, namely V_L.

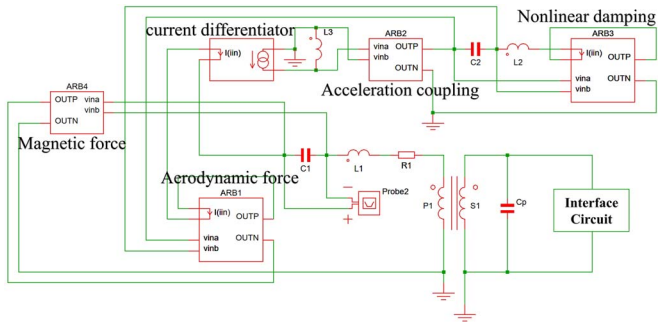

Fig. 7. ECM of the nonlinear VIVPEH.

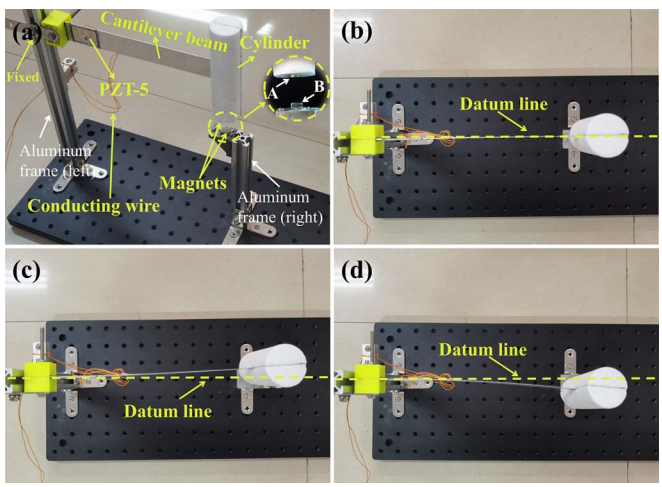

Fig. 8. (a) Physical prototype of the nonlinear VIVPEH. Two nonlinear configurations can be obtained by changing the vertical distance between the two small magnets: (b) monostable VIVPEH; (c) bistable VIVPEH (left equilibrium position); and (d) bistable VIVPEH (right equilibrium position).

Through the self-induction formula $V = L \times di/dt$, we can derive $\dot{y}(t) = V_L/L$ in (6), and the expression of ARB2 in (10) is based on this law.

By replacing the interface circuit block in Fig. 7 with ac, dc, or SSHI circuits, the effects of various interface circuits on the performance of the nonlinear VIVPEH can be analyzed and studied in the circuit simulation software.

IV. EXPERIMENTAL SETUP

Fig. 8 shows the prototype of the nonlinear VIVPEH used in this study. The equivalent lumped parameters of the prototype are identified and listed in Table II. The whole experimental apparatus is implemented on an optical breadboard. One end of the beam is fixed on a rigid support, and the piezoelectric transducer (PZT-5) is attached near the clamped end of the beam. The bluff body and the beam are assembled via a T-shaped connector. Detailed material properties and geometric parameters of the device components are listed in Table III. Monostable or bistable VIVPEHs can be obtained by changing the distance between magnets A and B. A monostable VIVPEH has a single equilibrium position, as shown in Fig. 8(b). As the name suggests, a bistable VIVPEH has two equilibrium positions, as shown in Fig. 8(c) and 8(d).

TABLE II
EQUIVALENT LUMPED PARAMETERS OF THE NONLINEAR VIVPEH

System Parameter	Symbol	Value	Unit
Effective mass	M_{eff}	6.034×10^{-3}	kg
Effective stiffness	K_{eff}	9.600	N/m
Damping ratio	ξ	0.013	/
Effective damping	C_{eff}	6.413×10^{-3}	Ns/m
Open-circuit natural frequency	f_{on}	6.349	Hz
Short-circuit natural frequency	f_{sn}	6.298	Hz
Air density	ρ	1.204	kg/m^3
Piezoelectric capacitance	C_p	41.782	nF
Electromechanical coupling coefficient	θ	3.226×10^{-5}	N/V
Experimental parameters	λ, A	0.3, 12	/

TABLE III
MATERIAL PROPERTIES AND GEOMETRIC PARAMETERS OF THE NONLINEAR VIVPEH

Device Component	Material Property	Geometric Parameter	
		Length × Width × Height (mm)	Diameter × Height (mm)
Installation base	Standard honeycomb optical breadboard	600 × 200 × 130	\
Aluminum frame (left)	Aluminium alloy (Euro 2020)	20 × 20 × 220	\
Cantilever beam	1060 pure aluminum	220 × 25 × 0.5	\
Cylindrical bluff body	Rigid foam (ρ=18 kg/m^3)	\	32 × 120
Piezoelectric ceramic	PZT-5	30 × 20 × 0.4	\
Aluminum frame (right)	Aluminium alloy (Euro 2020)	20 × 20 × 120	\
Magnet A	\	\	10 × 2
Magnet B	\	9 × 9 × 4	\

TABLE IV
NONLINEAR RESTORING FORCE COEFFICIENTS AT DIFFERENT DISTANCES

d (mm)	k_1 (N/m)	k_3 (N/m^3)
23	13.38	22 26.66
21	12.80	37 85.56
19	13.54	44 41.72
11	−2.48	365 34.00
9	−5.83	367 18.40
7	−12.21	385 62.90

V. RESULTS AND DISCUSSIONS

A. Experimental Validation

Before the wind tunnel test, an empirical function is fitted to describe the nonlinear magnetic force in (9) first. We first measured the forces exerted on the bluff body by the side magnet at different positions. Then, the least squares method was employed to fit the data to generate a third-order odd polynomial. In this way, the coefficients k_1 and k_3 in (9) are determined. Given different initial distances (d) between the two magnets, Table IV lists the identified coefficients of the fitting functions.

Fig. 9 shows the potential energy (E_p) of the VIVPEHs with different magnet distances, which is obtained by integrating the restoring force over a period of displacement, $E_p = \int_{-x_0}^{x_0} F_r(y)dy$. The potential energy plots of the three monostable cases (d = 23, 21, and 19 mm) are presented in Fig. 9(a). The concave bottom of the potential curve indicates a single equilibrium, and the linear stiffness primarily dominates the flatness of the bottom. As depicted in Fig. 9(b), two potential wells formed in all three bistable cases. Compared to monostable, bistable requires a higher cut-in wind speed.

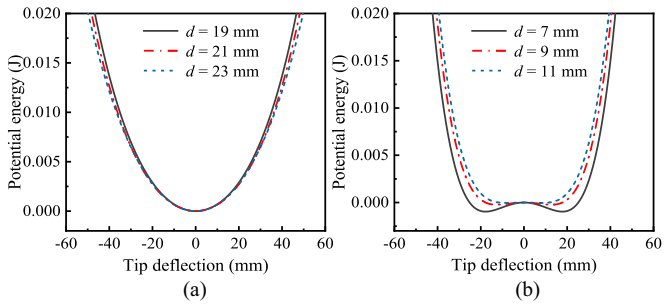

Fig. 9. Potential energy functions of nonlinear VIVPEHs: (a) three monostable cases: d = 23 mm, d = 21 mm, and d = 19 mm; and (b) three bistable cases: d = 11 mm, d = 9 mm, and d = 7 mm.

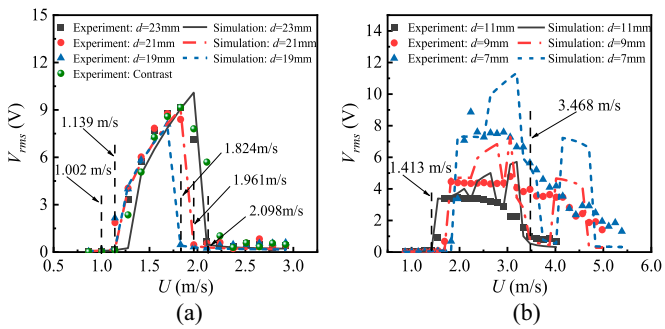

Fig. 10. Voltage response of the nonlinear VIVPEHs: rms OC voltage versus the wind speed, where the scattered points are experimental data, and the solid lines are ECM simulation results: (a) monostable configurations; and (b) bistable configurations.

Fig. 10 shows the rms open circuit (OC) voltage of the nonlinear VIVPEH with different d and subjected to different wind speeds. The scattered points in the figure are experimental data, and solid lines are ECM simulation results. Fig. 10(a) shows that the cutting wind speed measured by VIVPEH with d = 23 mm under experimental conditions is 1.139 m/s, and the working bandwidth is 1.133–2.098 m/s. And the simulation results show that the cut-in wind speed is 1.276 m/s, and the bandwidth is 1.276–2.098 m/s. For VIVPEH with d = 21 and 19 mm, the cut-in wind speed is 1.002 m/s, while the bandwidth is 1.002–1.961 and 1.002–1.824 m/s, respectively. In the simulation conditions, the VIVPEH cutting wind speed of the two conditions also showed consistency, both of which were 1.139 m/s, and the bandwidths were 1.139–1.961 and 1.139–1.824 m/s, respectively.

Fig. 10(b) clearly shows that compared with the monostable configurations, the operation bandwidths of the bistable ones are significantly enlarged. Among the three bistable cases, the operation bandwidth of the one with d = 11 mm is relatively narrow, i.e., 1.413–3.468 m/s, and its cutting wind speed is 1.413 m/s.

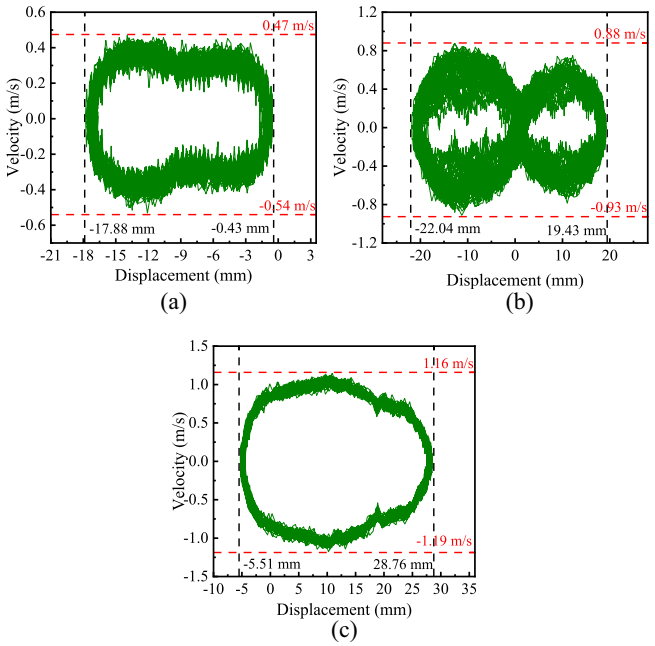

Fig. 11. Phase trajectory diagrams of the nonlinear VIVPEH at wind speed $U = 2.372$ m/s and with: (a) $d = 11$ mm; (b) $d = 9$ mm; and (c) $d = 7$ mm.

Even in the worst bistable case ($d = 11$ mm), the operation bandwidth is about 114.3% larger than that of the best monostable configuration ($d = 23$ mm). The solid lines in Fig. 10 represent the ECM simulation results. The established ECM effectively captures the dynamic characteristics of the monostable systems. However, the ECM cannot provide a highly accurate prediction of the amplitudes. The mismatch between the bistable results in Fig. 10(b) is mainly due to the multisolution problem of nonlinear systems. In the wind tunnel experiment, the wind speed changes slowly, which makes the experimental results in Fig. 10(b) relatively stable and smooth. However, the change in the initial conditions can lead to an abrupt jump between high- and low-orbit solutions. The dynamics of the bistable VIVPEHs will be analyzed in detail in the next section.

B. Output Performance Analysis

Fig. 11 displays the phase trajectory diagrams of the bistable VIVPEH system, obtained from the experiment conducted at a wind speed of 2.372 m/s and with different d. It can be seen that when $d = 11$ mm, the VIVPEH oscillates in the left potential well. The displacement is confined within -17.88–-0.43 mm, and the velocity range is -0.54–0.47 m/s. When $d = 9$ mm, interwell oscillation occurs: the oscillation falls within -22.04–19.43 mm, and the velocity is -0.93–0.88 m/s. When $d = 7$ mm, the VIVPEH oscillates in the right potential well: the vibration displacement spans over -5.51–28.76 mm, and the velocity is -1.19–1.16 m/s. It is evident that the displacement and velocity amplitudes of the VIVPEH increase as d decreases, as the reduction in d results in the bistable system experiencing greater negative stiffness and increased oscillation under the same input conditions.

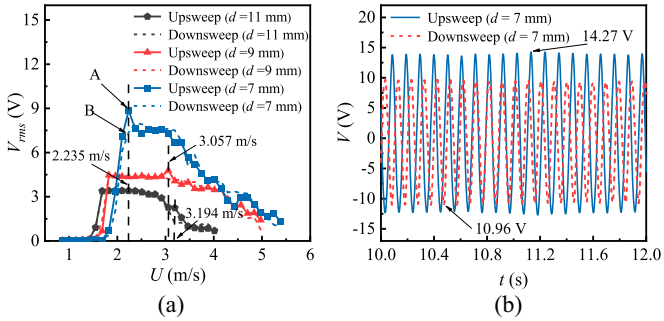

Fig. 12. (a) Variation of the rms OC voltage of the VIVPEH with the increase or decrease of the wind speed. (b) Time-history voltage responses at points A and B.

Fig. 12(a) plots the rms OC voltage of the nonlinear VIVPEH versus the wind speed. The wind speed was up- and downswept in the experiment. It can be noted that the bistable VIVPEH with $d = 11$, 9, and 7 mm produced different output voltage values at 3.194, 3.057, and 2.235 m/s, respectively, in the wind speed sweeping tests. In Fig. 12(a), two points A and B represent the steady-state responses achieved in the upsweep and downward sweeping tests when $U = 2.235$ m/s. Fig. 12(b) presents the time-history voltage responses at points A and B in Fig. 12(a). In the upsweeping test, the voltage amplitude achieved at point A is 14.27 V, while the voltage attained at point B in the downward sweeping process is 10.96 V. 14.27 V and 10.96 V are the peak instantaneous voltage amplitudes at the two working conditions A and B in the period of 10–12 s. Given different initial conditions, the nonlinear VIVPEH reaches different steady states at the same wind speed. In other words, different initial conditions can lead to entirely different results at the same wind speed, which is the typical bifurcation phenomenon of nonlinear systems.

C. Comparison of Different Circuits

1) AC Circuit: As validated above, the ECM can capture the dynamics of a monostable VIVPEH. This section investigates the rms voltage, average power, and tip displacement of the monostable VIVPEH ($d = 23$ mm) shunted to an ac circuit and subjected to wind speeds of 1.413, 1.687, 1.961, and 2.235 m/s. It can be observed from Fig. 13(a) that with the increase of the load resistance, the rms voltage first shows rapid growth, followed by a gradual convergence to the OC voltage. It can be seen in Fig. 13(b) that the average power first increases and then decreases with the load resistance, and the optimal load (R_{opt}) is about 0.5 MΩ. When $U = 1.961$ m/s, the max average power is 123 μW. At a wind speed of 2.235 m/s, outside the lock-in zone, the output power of the VIVPEH decreases dramatically. As shown in Fig. 13(c), the displacement of the VIVPEH changes slightly with the load resistance. The displacement demonstrates noticeable changes only near the optimal load of 0.5 MΩ: it decreases first and then increases. The minimum displacement is attained at the optimal load since the electrical damping effect at the optimal load is enhanced. The differences between the maximum and the minimum displacements under the four wind speeds are about 0–0.41 mm.

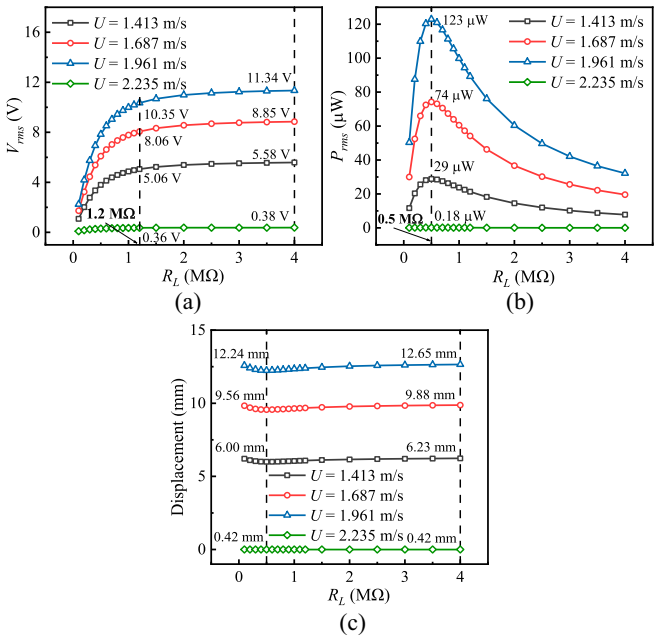

Fig. 13. Responses of the nonlinear VIVPEH (d = 23 mm) shunted to an ac interface circuit with different load resistances: (a) rms output voltage; (b) average output power; and (c) tip displacement.

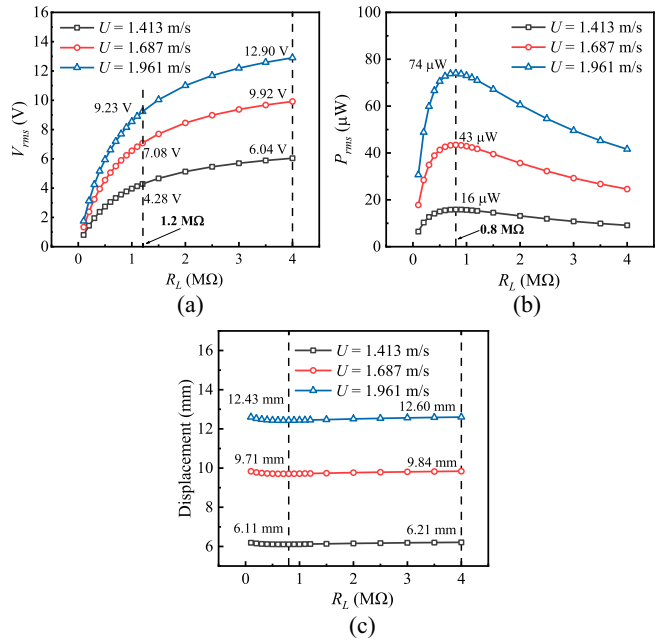

Fig. 15. Responses of the nonlinear VIVPEH shunted to a dc interface circuit at different load resistances: (a) rms output voltage; (b) average output power; and (c) vibration amplitude.

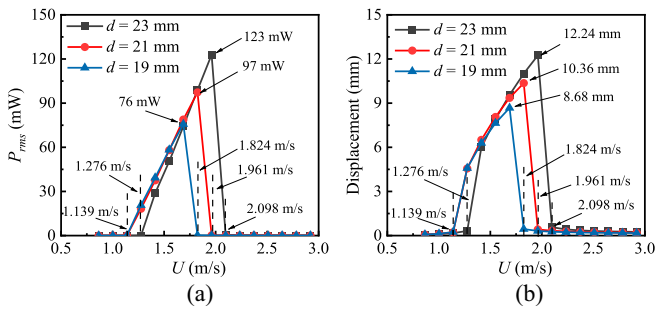

Fig. 14. Responses of the nonlinear VIVPEH configured with different d and shunted to an ac interface circuit at different wind speeds: (a) average output power; and (b) displacement amplitudes.

Based on the above research, we delve into studying the output responses of the nonlinear VIVPEH configured in three monostable states (d = 23, 21, and 19 mm) and shunted to an ac circuit at the optimal load R_{opt} = 0.5 MΩ. The results are shown in Fig. 14. It can be seen that with the increase of the wind speed, the output power first increases and then decreases in the lock-in range when d = 23 mm, and the working bandwidth is 1.276–2.098 m/s and the maximum average power produced is 123 μW. In the case of d = 21 mm, the working bandwidth of the VIVPEH is 1.139–1.961 m/s, and the maximum average power is 97 μW. When d is adjusted to 19 mm, the working bandwidth becomes 1.139–1.824 m/s, with a maximum average power of 76 μW. Fig. 14(b) shows the displacement amplitude response of the VIVPEH as a function of the wind speed. It is observed that the maximum amplitudes of the three configurations with d = 23, 21, and 19 mm are 12.24, 10.36, and 8.68 mm, respectively. The nonlinear VIVPEH produces a larger output power at d = 23 mm due to its wider potential energy well, and the bluff body can oscillate more intensively.

2) DC Circuit: This section considers the VIVPEH shunted to a dc circuit. Fig. 15 shows the output response of the nonlinear VIVPEH configured in the monostable state (d = 23 mm). It can be observed in Fig. 15(a) that the rms voltage gradually increases as the load resistance increases. When R_L = 4 MΩ, the voltage outputs produced at the wind speeds of 1.413, 1.687, and 1.961 m/s are, respectively, 6.04, 9.92, and 12.90 V, which are higher than the voltage outputs of the monostable VIVPEH shunted to an ac interface circuit under the same working condition. It can be seen in Fig. 15(b) that the average power increases first and then decreases with the load resistance, and the optimal load resistance is R_{opt} = 0.8 MΩ. The corresponding optimal power of the monostable VIVPEH at the three different wind speeds is 16, 43, and 74 μW, respectively. Unlike the rms voltage, the optimal power outputs are lower than those when shunted to an ac interface circuit under the same working condition. This occurs because the rectifier bridge in the standard dc circuit dissipates energy. The optimal load of the monostable VIVPEH using a dc circuit is 1.6 times larger than that shunted to an ac circuit. Fig. 15(c) shows the change of the monostable VIVPEH displacement with the load resistance. The displacement-varying trend of the case using a dc circuit is similar to that of the case with an ac circuit. The range of differences between maximum and minimum displacements at the three wind speeds is approximately 0.1–0.17 mm, notably smaller than the displacement variations induced by the ac circuit.

Fig. 16 illustrates the variations in power output and vibration amplitude for the monostable VIVPEH system when shunted to a dc circuit, optimized with a resistance value of R_{opt} = 0.8 MΩ,

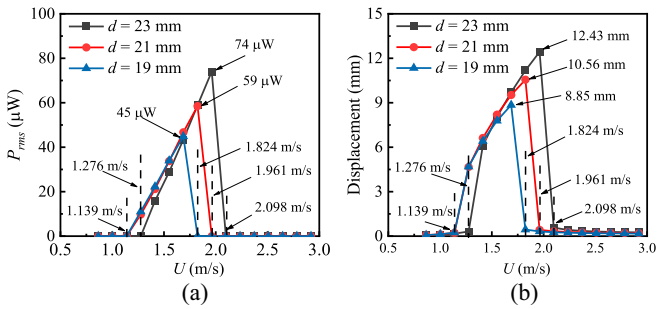

Fig. 16. Responses of the nonlinear VIVPEH configured with different d and shunted to a dc interface circuit at different wind speeds: (a) average output power; and (b) displacement response.

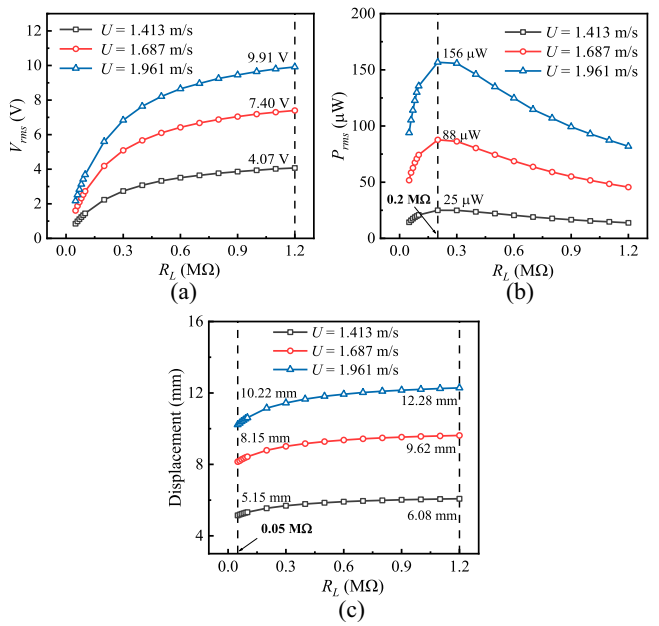

Fig. 17. Responses of the monostable VIVPEH shunted to an S-SSHI interface circuit at different wind speeds: (a) rms output voltage; (b) average output power; and (c) displacement response.

across a range of wind speeds. It can be seen in Fig. 16(a) that compared with the monostable VIVPEH connected to an ac circuit, the vibration amplitudes and the working bandwidth of the one connected to a dc circuit slightly changed. However, the power output amplitudes significantly decreased. At $d = 23$, 21, and 19 mm, the monostable VIVPEH connected to a dc circuit generates average power outputs of 74, 59, and 45 μW, respectively. These outputs are 39.8%, 39.18%, and 40.79% lower than those harnessed by the VIVPEH connected to an ac circuit under the same working conditions. Fig. 16(b) shows the response amplitude of the monostable VIVPEH versus the wind speed. The maximum amplitudes are 12.43, 10.56, and 8.85 mm, respectively, when $d = 23$, 21, and 19 mm. The displacement results are not much different from the ones used in the case of an ac interface circuit.

3) SSHI Circuits: Fig. 17 shows how the output response of the monostable VIVPEH ($d = 23$ mm) shunted to an S-SSHI circuit changes with the load resistance at different wind speeds. It can be seen in Fig. 17(a) that the rms voltage gradually increases with the increase of the load resistance. At $R_L = 1.2$ MΩ, the voltage outputs of the monostable VIVPEH at the wind speeds of 1.413, 1.687, and 1.961 m/s are 4.07, 7. 40, and 9.91 V, respectively. Under the same working conditions, the voltage outputs produced by the monostable VIVPEH using the S-SSHI circuit are smaller than those with the ac circuit. This is because some electrical components, including diodes and transistors, are in the S-SSHI circuit, and they consume additional electric energy and cause voltage drops. It can be noted in Fig. 17(b) that with the increase of the load resistance, the power output first increases and then decreases, and the optimal power is achieved at $R_{opt} = 0.2$ MΩ. The average power outputs at R_{opt} under the wind speeds of 1.413, 1.687, and 1.961 m/s are 25, 88, and 156 μW, respectively, which are higher than the optimal power outputs harvested by the dc circuit.

When the wind speed is 1.413 m/s, the power output harvested by the ac circuit is larger than that by the S-SSHI circuit. However, as the wind increases and achieves 1.687 and 1.961 m/s, the S-SSHI circuit outperforms the ac circuit. The reason is that, at low-wind speeds, the voltage drops across the diodes and transistors within the self-powered S-SSHI circuit become significant, comparable to the voltage across the piezoelectric transducer. This comparability results in nonnegligible energy dissipation within these components. As the wind speed rises, the voltage across the piezoelectric transducer increases, and the voltage drops on the diodes and transistors become insignificant. In general, the efficiency-boosting effect of the S-SSHI circuit is achieved at around the peak of the lock-in region. For a more vivid illustration, at a wind speed of 1.961 m/s, the nonlinear VIVPEH shunted to the S-SSHI interface circuit produces a maximum power output of 156 μW. This power output is 26.83% higher than that obtained with an ac circuit and significantly surpasses the output from a dc circuit by 110.81%. Fig. 17(c) shows the change of the vibration amplitudes of the nonlinear VIVPEH with the load resistance: the displacement amplitude gradually increases with the increase of the load resistance.

Fig. 18 shows the output responses of the monostable VIVPEH shunted to a P-SSHI interface circuit with varying resistances and under different wind speeds. Fig. 18(a) demonstrates that the rms voltage gradually increases with the load resistance. Given $R_L = 1.2$ MΩ, the voltage outputs at the wind speeds of 1.413, 1.687, and 1.961 m/s are 6.47, 11.33, and 14.93 V, respectively, which are higher than the voltage outputs of the S-SSHI circuit under the same working condition. Fig. 18(b) depicts that with the increase of the load resistance, the power output first increases and then decreases, and achieves the maximum at the optimal load of $R_{opt} = 2$ MΩ. The average power outputs harnessed at R_{opt} under the wind speeds of 1.413, 1.687, and 1.961 m/s are 38, 117, and 203 μW, respectively, which are higher than the optimal power outputs of the ac, dc, and S-SSHI circuits under the same working condition. For instance, when the wind speed is 1.961 m/s, the maximum power output harvested by the P-SSHI circuit is 203 μW, which is 65.04%, 174.32%, and 30.13% higher than those of the ac, dc, and S-SSHI

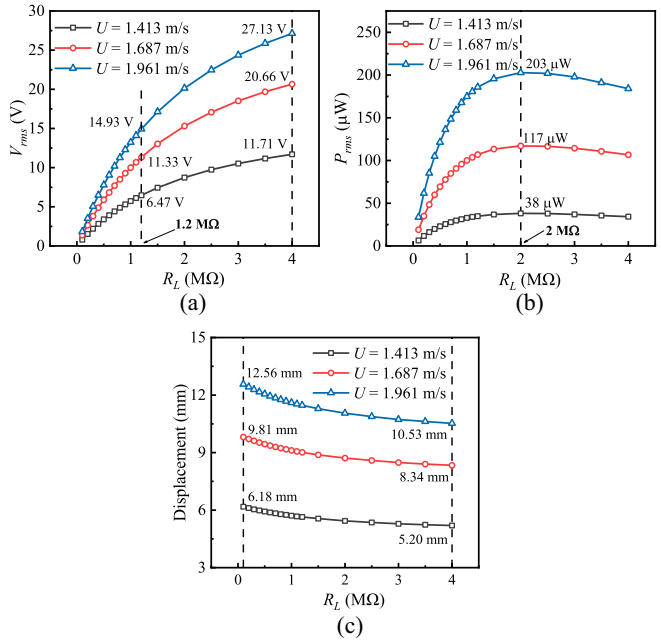

Fig. 18. Responses of the monostable VIVPEH shunted to a P-SSHI interface circuit at different wind speeds: (a) rms output voltage; (b) average output power; and (c) displacement response.

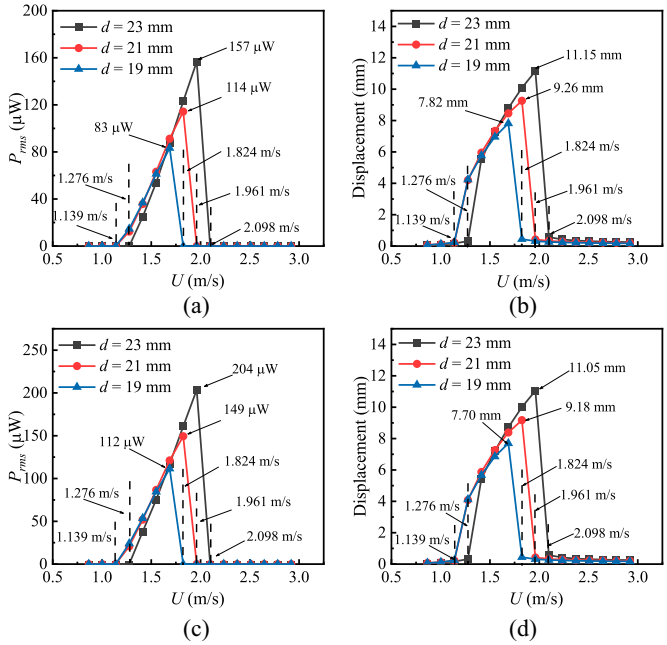

Fig. 19. Responses of the monostable VIVPEH shunted to SSHI circuits under different wind speeds: (a) average output power of the S-SSHI; (b) displacement response of the S-SSHI; (c) average output power of the P-SSHI; and (d) displacement response of the P-SSHI.

circuits, respectively. Fig. 18(c) shows the vibration amplitudes of the monostable VIVPEH as the load resistance changes. The displacement amplitude gradually decreases with the increase of the load resistance. One can observe that the displacement response characteristics of the energy harvester shunted to the SSHI circuits differ from those shunted to the ac and dc circuits at the optimal loads. This discrepancy arises because the ac and dc interface circuits are simpler in comparison. In the ideal scenario where the rectifier bridge has no voltage drops, the energy harvested equals the energy dissipated in the ac and dc circuits, resulting in maximum electrical damping when impedance matching is achieved. However, the SSHI circuits have more intricate topologies, incorporating passive elements with nonnegligible energy consumption and energy dissipation during switching operations. Consequently, the electrical-induced damping in the SSHI circuits is influenced not only by harvested energy but also by energy dissipation in passive elements and during switching operations. Therefore, while impedance matching may optimize power harvesting, it may not necessarily correspond to the highest electrical-induced damping to achieve maximum vibration attenuation.

Fig. 19 shows the power and displacement amplitudes of the monostable VIVPEH (configured with different d) shunted to two SSHI circuits under different wind speeds and at the corresponding optimal loads $R_{opt} = 0.2$ MΩ and $R_{opt} = 2$ MΩ. The results are similar to those of the ac and dc circuits regarding the varying trends, the cut-in wind, and the operating bandwidths. However, in terms of the amplitude, as revealed in Fig. 19(a) and 19(c), the maximum average power outputs harnessed by the S-SSHI circuit are 83, 114, and 157 μW when $d = 23$, 21, and 19 mm, respectively. Under the three same working conditions, the P-SSHI circuit produces significantly higher average power outputs of 112, 149, and 204 μW than the ac and dc circuits. The power outputs of the monostable VIVPEH shunted to the P-SSHI circuit are greater than those of the S-SSHI circuit at the same wind speed. Fig. 19(b) and 19(d) shows how the vibration amplitudes of the monostable VIVPEH change with the wind speed. They demonstrate that the vibration amplitudes of the monostable VIVPEH using the two SSHI circuit interfaces are nearly identical at the same wind speed.

VI. Conclusion

This article presents the design and analysis of a nonlinear PEH for VIV energy harvesting. The nonlinear force is introduced using two small magnets configured to produce repulsive force. First, the conceptual design of the VIVPEH with different nonlinearities was presented, the experimental prototype was fabricated, and the wind tunnel experiment was carried out. The bistable characteristics were studied via experiments. Subsequently, based on the equivalent circuit representation, the nonlinear mass-spring-damper system is transformed into an inductor–capacitor–resistor circuit model to realize system-level simulation and performance analysis. The experimental results qualitatively agree with the predicted results regarding the operating bandwidth, OC voltage level, and voltage variation trend. Finally, the nonlinear VIVPEH was shunted to simple ac, standard dc, and SSHI interface circuits. The results are analyzed and compared to unveil the effects of different circuits on the operational wind speed bandwidth, power outputs, and vibration amplitudes.

Some key findings are summarized as follows. The nonlinear design can significantly enlarge the working bandwidth of the VIVPEH, with the bistable configuration at least 114.3% larger than the monostable configuration. In bistable VIVPEHs, increasing d leads to increased amplitude and potentially multistable behavior. The self-powered S-SSHI circuit significantly outperforms the traditional ac and dc circuits at high-wind speeds while not at low-wind speeds. Specifically, when the wind speed is 1.961 m/s, the output power of the VIVPEH shunted to the P-SSHI circuit is 65.04% and 174.32% higher than that shunted to the ac and dc circuits, respectively. In addition, the two SSHI circuits reach their maximum output power at different load resistors: S-SSHI at 0.2 MΩ and P-SSHI at 2 MΩ. It is worth mentioning that with the ability to adjust the resistance value of the three voltage regulator resistors in the SSHI circuit, it is possible to maintain the output voltage while ensuring high-power output. Further studies can be conducted to optimize the SSHI circuit.

REFERENCES

[1] K. Tao et al., "Origami-inspired electret-based triboelectric generator for biomechanical and ocean wave energy harvesting," *Nano Energy*, vol. 67, 2020, Art. no. 104197.

[2] S. Wang et al., "Energy harvesting from water impact using piezoelectric energy harvester," *Rev. Sci. Instrum.*, vol. 95, no. 2, 2024, Art. no. 021501.

[3] H. Zhu, G. Li, and J. Wang, "Flow-induced vibration of a circular cylinder with splitter plates placed upstream and downstream individually and simultaneously," *Appl. Ocean Res.*, vol. 97, 2020, Art. no. 102084.

[4] A. Mehmood et al., "Piezoelectric energy harvesting from vortex-induced vibrations of circular cylinder," *J. Sound Vib.*, vol. 332, no. 19, pp. 4656–4667, 2013.

[5] J. Kan et al., "Enhanced piezoelectric wind-induced vibration energy harvester via the interplay between cylindrical shell and diamond-shaped baffle," *Nano Energy*, vol. 89, 2021, Art. no. 106466.

[6] J. Wang et al., "Exploring the potential benefits of using metasurface for galloping energy harvesting," *Energy Convers. Manage.*, vol. 243, 2021, Art. no. 114414.

[7] J. M. McCarthy et al., "Fluttering energy harvesters in the wind: A review," *J. Sound Vib.*, vol. 361, pp. 355–377, 2016.

[8] L. Grainger, D. Rezgui, and D. Barton, "Optimisation of an aeroelastic flutter energy harvester," in *Proc. 58th AIAA/ASCE/AHS/ASC Struct. Struct. Dyn. Mater. Conf.*, 2017, pp. 1–11.

[9] J. Wang et al., "Broadening band of wind speed for aeroelastic energy scavenging of a cylinder through buffeting in the wakes of a squared prism," *Shock Vib.*, vol. 2018, pp. 1–14, 2018.

[10] M. Armandei and A. C. Fernandes, "Marine current energy extraction through buffeting," *Int. J. Mar. Energy*, vol. 14, pp. 52–67, 2016.

[11] J. Wang et al., "High-performance piezoelectric wind energy harvester with Y-shaped attachments," *Energy Convers. Manage.*, vol. 181, pp. 645–652, 2019.

[12] A. Barrero-Gil, S. Serruys, and A. Velazquez, "Influence of cross-section shape on energy harvesting from transverse flow-induced vibrations of bluff bodies," *J. Fluid Mech.*, vol. 950, 2022.

[13] J. Xing et al., "Investigating the coupled effect of different aspect ratios and leeward protrusion lengths on vortex-induced vibration (VIV)-galloping energy harvesting: Modelling and experimental validation," *J. Sound Vib.*, vol. 568, 2024, Art. no. 118054.

[14] L. He et al., "A piezoelectric-electromagnetic hybrid energy harvester for low-frequency wave motion and self-sensing wave environment monitoring," *Energy Convers. Manage.*, vol. 300, 2024, Art. no. 117920.

[15] Y. Peng et al., "Toward highly sensitive ocean-wave monitoring with sliding-triboelectric effect: Modeling, experimental validation, and demonstration," *IEEE/ASME Trans. Mechatron.*, early access, Apr. 2024, doi: 10.1109/TMECH.2024.3382368.

[16] S. Fang et al., "Theoretical and experimental investigation on the advantages of auxetic nonlinear vortex induced vibration energy harvesting," *Appl. Energy*, vol. 356, 2024, Art. no. 122395.

[17] S. Zhou, B. Yan, and D. J. Inman, "A novel nonlinear piezoelectric energy harvesting system based on linear-element coupling: Design, modeling and dynamic analysis," *Sensors (Basel)*, vol. 18, no. 5, p. 1492, 2018.

[18] M. Belhaq et al., "Homotopy analysis approach for nonlinear piezoelectric vibration energy harvesting," in *Proc. MATEC Web of Conf.*, 2016, p. 83.

[19] A. Bibo, A. H. Alhadidi, and M. F. Daqaq, "Exploiting a nonlinear restoring force to improve the performance of flow energy harvesters," *J. Appl. Phys.*, vol. 117, no. 4, 2015, Art. no. 045103.

[20] H.-T. Li et al., "Improving the galloping energy harvesting performance with magnetic coupling," *Int. J. Mech. Sci.*, vol. 237, 2023, Art. no. 107785.

[21] L. He et al., "Research-based on a low-frequency non-contact magnetic coupling piezoelectric energy harvester," *Energy*, vol. 258, 2022, Art. no. 124844.

[22] Y. Han et al., "Composite piezoelectric-electromagnetic synchronously powering and sensing device for vehicle monitoring," *Energy Convers. Manage.*, vol. 286, 2023, Art. no. 117040.

[23] Y. Yang and L. Tang, "Equivalent circuit modeling of piezoelectric energy harvesters," *J. Intell. Mater. Syst. Struct.*, vol. 20, no. 18, pp. 2223–2235, 2009.

[24] K. Tao et al., "Investigation of multimodal electret-based MEMS energy harvester with impact-induced nonlinearity," *J. Microelectromech. Syst.*, vol. 27, no. 2, pp. 276–288, 2018.

[25] L. Tang et al., "Equivalent circuit representation and analysis of galloping-based wind energy harvesting," *IEEE/ASME Trans. Mechatron.*, vol. 20, no. 2, pp. 834–844, Apr. 2015.

[26] L. Zhao, L. Tang, and Y. Yang, "Synchronized charge extraction in galloping piezoelectric energy harvesting," *J. Intell. Mater. Syst. Struct.*, vol. 27, no. 4, pp. 453–468, 2015.

[27] A. B. Daniel Guyomar, E. Lefeuvre, and C. Richard, "Toward energy harvesting using active materials and conversion improvement by nonlinear processing," *IEEE Trans. Ultrason., Ferroelectr., Freq. Control*, vol. 52, no. 4, pp. 584–595, Apr. 2005.

[28] L. Zhao, J. Liang, L. Tang, Y. Yang, and H. Liu, "Enhancement of galloping-based wind energy harvesting by synchronized switching interface circuits," in Proc. *Active and Passive Smart Structures and Integrated Systems*, Apr. 2015, Art. no. 94310E.

[29] I. C. Lien et al., "Revisit of series-SSHI with comparisons to other interfacing circuits in piezoelectric energy harvesting," *Smart Mater. Struct.*, vol. 19, no. 12, p. 19, 2010.

[30] J. Wang et al., "Equivalent circuit representation of a vortex-induced vibration-based energy harvester using a semi-empirical lumped parameter approach," *Int. J. Energy Res.*, vol. 44, no. 6, pp. 4516–4528, 2020.

[31] J. Jia et al., "Equivalent circuit modeling and analysis of aerodynamic vortex-induced piezoelectric energy harvesting," *Smart Mater. Struct.*, vol. 31, no. 3, 2022.

[32] W. Liu et al., "A comprehensive analysis and modeling of the self-powered synchronous switching harvesting circuit with electronic breakers," *IEEE Trans. Ind. Electron.*, vol. 65, no. 5, pp. 3899–3909, May 2018.

[33] H. Fu and E. M. Yeatman, "Effective piezoelectric energy harvesting using beam plucking and a synchronized switch harvesting circuit," *Smart Mater. Struct.*, vol. 27, no. 8, 2018, Art. no. 084003.

[34] G. Hu, J. Wang, and L. Tang, "A comb-like beam based piezoelectric system for galloping energy harvesting," *Mech. Syst. Sig. Process.*, vol. 150, 2021.

[35] G. Hu et al., "Modelling of a cantilevered energy harvester with partial piezoelectric coverage and shunted to practical interface circuits," *J. Intell. Mater. Syst. Struct.*, vol. 30, no. 13, pp. 1896–1912, 2019.

[36] M. L. Facchinetti, E. de Langre, and F. Biolley, "Coupling of structure and wake oscillators in vortex-induced vibrations," *J. Fluids Struct.*, vol. 19, no. 2, pp. 123–140, 2004.

[37] J. E. Kim, "On the equivalent mass-spring parameters and assumed mode of a cantilevered beam with a tip mass," *J. Mech. Sci. Technol.*, vol. 31, no. 3, pp. 1073–1078, 2017.

[38] M. Gürgöze, "On the representation of a cantilevered beam carrying a tip mass by an equivalent spring–mass system," *J. Sound Vib.*, vol. 282, no. 1–2, pp. 538–542, 2005.

Junlei Wang received the B.E. and Ph.D. degrees in power and engineering thermophysics from the School of Power Engineering, Chongqing University, Chongqing, China, in 2009 and 2014, respectively.

Currently, he is a Professor with the School of Mechanical and Power Engineering, Zhengzhou University, Zhengzhou, China. He was a Visiting Scholar in mechanical engineering with The University of Auckland, Auckland, New Zealand, from 2019 to 2020. His research interests include flow-induced vibrations suppression, flow energy harvesting, and triboelectric, piezoelectric, and hybrid energy harvesting technologies.

Liangjun Luo received the B.E. degree in nuclear engineering and technology from Three Gorges University, Yichang, China, in 2018. Currently, she is working toward the master's degree with the School of Mechanical and Power Engineering, Zhengzhou University, Zhengzhou, China.

Her research interests include flow-induced vibration suppression, flow energy harvesting, and piezoelectric and hybrid energy harvesting technologies.

Daniil Yurchenko received the Ph.D. degree in mechanical engineering from Worcester Polytechnic Institute, Worcester, MA, USA.

He is a currently a Member of the EUROMECH and IFToMM, Editorial Board Member managing a work flow for Mechanical Systems and Signal Processing, Vibration, International Journal of Dynamics and Control. In 2021, he joined the Institute of Sound and Vibration Research, University of Southampton, Southampton, Hampshire, UK. In 2007, he was a Full Professor with the Department of Mathematical Sciences, St. Peterburg State Polytechnic University, St. Petersburg, Russia. He has published over 150 scientific publications, including peer-reviewed journals and conference proceedings.

Dr. Yurchenko received the Young Scientists Award from the Russian President Science Council, in 2008. He is an Editorial Board Member of *Mechanical Systems and Signal Processing*, *International Journal of Dynamics and Control*, *Journal of Vibration Testing and System Dynamics*, *Vibrations*, and *Energies*.

Guobiao Hu received the B.Eng. degree in mechanical engineering from the Southwest Jiaotong University, Chengdu, China, in 2012, the Diplôme d'Ingénieur in general engineering from École Centrale Paris, Châtenay-Malabry, France, in 2015, and the Ph.D. degree in mechanical engineering from The University of Auckland, Auckland, New Zealand, in 2020.

Currently, he is a tenure-track Assistant Professor with the Internet of Things Thrust, Information Hub, The Hong Kong University of Science and Technology, Guangzhou, China. His research interests include vibration/wind energy harvesting and acoustic–elastic metamaterials.